Volume 21
Number 1

December *2019*
(ISSN 1109-1606)

Journal of

APPLIED ELECTROMAGNETISM

JAE

Institute of Communication and Computer Systems

Athens - GREECE

Volume 21 **December 2019**
Number 1 **(ISSN 1109-1606)**

JOURNAL
OF
APPLIED ELECTROMAGNETISM

Institute of Communication and Computer Systems

Athens - GREECE

Volume 21 **Number 1**

December 2019

TRANS BLACK SEA REGION UNION OF APPLIED ELECTROMAGNETISM (BSUAE)

JOURNAL OF APPLIED ELECTROMAGNETISM

Institute of Communication and Computer Systems

Athens - GREECE

Journal of Applied Electromagnetism

Copyright Form

The undersigned I confirm that I agree the publication of the article

in the Journal of Applied Electromagnetism and the copyright to belong to Trans Black Sea Union of Applied Electromagnetism. I understand that I have the full right to reuse this manuscript for my own purposes.

Name:

Surname:

Address:

E-mail:

Signed:

***Please send the previous form signed either by e-mail to pfrangos@central.ntua.gr , or by fax to the fax number: +30 210 772 2281, attention of Prof. P. Frangos.**

Address

Institute of Communication and Computer Systems,

National Technical University of Athens,

9, Iroon Polytechniou Str.,

157 73 Athens - GREECE

Tel: (+30) 210 772 3694

Fax: (+30) 210 772 2281, attention of Prof. P. Frangos

e-mail: pfrangos@central.ntua.gr

Web site: **http://jae.ece.ntua.gr**

TRANS BLACK SEA REGION UNION OF APPLIED ELECTROMAGNETISM (BSUAE)

JOURNAL OF APPLIED ELECTROMAGNETISM (JAE)

Volume 21 Number 1 December 2019

CONTENTS

Radiotherapy is one of the most effective treatments for breast cancer. Three-dimensional conformal radiotherapy (3D-CRT) and Volumetric modulated Arc therapy(VMAT) are 2 recently developed radiotherapy techniques .This paper aims to compare dosimetric differences based on three types of radiotherapy plans for postoperative left breast cancer. In particular, based on a clinical dosimetric study, the three-dimensional conformal radiotherapy (3D-CRT), and VMAT plans were implemented on 7 cases of postoperative patients with left breast cancer with prescription doses of 4000cGy.

Over water microwave propagation is often affected by the presence of evaporation duct. The tropospheric ducting is one of the major causes for multipath propagation. The ducting propagation mechanism is known to be highly frequency dependent whereas the prediction methods for multipath fading distribution suggest a rather slight dependence on frequency. In order to check this discrepancy, the paper studies the influence of the variations of important parameters of the evaporation duct log-linear refractivity profile and the sea surface roughness on the frequency dependency of multipath fading. The refractivity profiles serve as input to the parabolic equation method which provides a full-wave solution to the path loss problem. The sea surface roughness is modelled through two roughness reduction factors, one of them accounting for the shadowing. Ten frequencies of microwave range are used in four hypothetical over the sea links. The results are presented in form of path loss standard deviation versus frequencies for fixed ranges.

COMPATISION BETWEEN VOLUMETRIC MODULATED ARC THERAPY (VMAT) AND 3D TANGENTIAL BEAMS TECHNIQUE USED IN PATIENTS WITH BREAST CANCER

Ketevan Kotetishvili, T.Gonashvili, Sh.Robitashvili

E-mail: k.kotetishvili@gtu.ge, t.gonashvili@gmail.com, robitashvili.shako@gmail.com

Abstract

Radiotherapy is one of the most effective treatments for breast cancer. Three-dimensional conformal radiotherapy (3D-CRT) and Volumetric modulated Arc therapy (VMAT) are 2 recently developed radiotherapy techniques. This paper aims to compare dosimetric differences based on three types of radiotherapy plans for postoperative left breast cancer. In particular, based on a clinical dosimetric study, the three-dimensional conformal radiotherapy (3D-CRT), and VMAT plans were implemented on 7 cases of postoperative patients with left breast cancer with prescription doses of 4000cGy.

1. INTRODUCTION AND PROBLEM FORMULATION

Radiation therapy has become one of the vital measurements of postoperative breast cancer treatment. It is also the most important means of improving the local control rate of tumor, as well as to reduce complication of the normal tissues. The radiotherapy technology is more complex, and in order to avoid overlap and omission of adjacent radiation, reducing radiation damage to normal tissue without missing the target area ought to be taken as a basic requirement for radiotherapy[1]. Conventionally, the 3D-CRT has been one of the typical main plan solutions. Our methods are based on breast tangential field irradiation and lymphatic draining region irradiation by using center irradiation method of tangent field. However, this comes with the disadvantages of poor target area fitness and higher complexity in our radiotherapy practice. The extensive treatment time would cause reduction of relative biological effects, postural changes of patients during treatment, decrease of treatment accuracy and a series of problems. With the rapid development of hardware and software in the field of radiotherapy, a new type of technology known as the Volumetric Modulated Arc Therapy (VMAT), which

combines the fixed field IMRT and pull arc irradiation, has been developed recently. Dosimetry studies show that VMAT can be better than the fixed field IMRT. The VMAT technology that is provided by Monaco treatment planning system has already been confirmed as VMAT. To achieve rotation IMRT treatment, this technology was used to calculate the state of multi-leaf collimator motion by adopting reverse optimization algorithm, meanwhile by optimizing the dose rate and rotate speed of the rack. Due to the arc structure of the breast cancer, three radiotherapy techniques, i.e., 3D-CRT, VMAT, have been widely applied in clinic nowadays. The purpose of this paper was to compare the dosimetric parameters and to obtain the most superior radiotherapy technique, i.e., to obtain the optimal dosimetric distribution of the target and to maximum reduce the dose delivered to the lung by designing three radiotherapy plans for a certain case. The purpose of this paper is to compare the intensity modulated radiotherapy (IMRT) with the 3D tangential beams technique in respect of dose distribution in target volume and critical organs they generate in patients with early-stage breast cancer who received breast-conserving therapy.

2. MATERIALS AND METHOD

2.1 Case Selection

We randomly selected 7 cases of postoperative radiotherapy for breast cancer in our hospital during Jun 2019. The patients are all female, aged 38 to 65 years old, the average age of 45 years old, and the primary lesions are left breast.

2.2 CT simulation location and target area delineation and definition

Patients raised one arms above their heads, and were fixed by elekta breast step. CT scans with a slice thickness of 3mm.CT scans ranges from the mandible to the thorax, which completely cover all the adjacent normal tissues and organs such as lung, heart, opposite breast and the spinal cord, etc. The clinical target volume (CTV), including the whole ipsilateral chest wall and lymph node region around collar bone, was outlined by the oncologist by using Monaco treatment planning system (TPS), and the organs at risk (OARs) including ipsilateral lung, contralateral lung, contralateral breast, heart, and the spinal cord were delineated then.

2.3 Plan design

The prescription dose given was 4000cGy, which was irradiated for 15 times, herein, for fractionated dose of 200cGy, 99% of CTV is supposed to receive at least 95% of prescription dose (3680cGy). Clinical constraints are as follows: CTV≤107%, the minimum dose≥95%, V20<30%, for heart and the dose delivered to the contralateral lung and the contralateral breast should be less as far as possible.

2.4 The two radiotherapy plans

Conventional 3D CRT treatment planning is manually optimized . This means that the treatment planner chooses all beams parameters, such as the number of beams, beam directions, shapes, weights etc., and the computer calculates the resulting dose distribution it using 6 MV X-ray,

VMAT: using 6 MV X-ray, double arc way (clockwise and counterclockwise) to disperse field, abduction of 10°-25° by tangent field as starting and ending angle each way, with collimator angle 5°, treatment couch angle 0°, maximum dose rate 600 MU/min, and algorithm model is AAA. In the process of designing, doses of cold and hot points were optimized and adjusted by defining dose shaping structure.

3. NUMERICAL RESULTS

VMAT is a kind of Rotational Intensity Modulated technology based on VMAT theory proposed by Otto[3]. The full arc frame can rotate about 360°. The arc consists of 177 control nodes, whereby the rotating speed of the frame is 4.8°/s. The maximum dose rate is 570 MU/min. MLC blade's maximum speed is 2.5 cm/s. Gantry rotation takes about 75 s per circle. Many scholars have done researches on VMAT in the body, the head and the neck. The results show that VMAT can reduce the total time of radiotherapy plan for patients and the beam-on time of the accelerator. The greatest advantage of VMAT technology is to further reduce the treatment time and the number of MU without reducing dose distribution, so as to improve the treatment target of biological effects and the number of patients treated in a unit of time[6-9]. Because the number of MU reduces obviously, thereby reducing the number of scattering lines of the accelerator head collimator, the risk of cancer reoccurrence is reduced theoretically.

The study compares two kinds of radiotherapy techniques for left breast cancer. These two treatments can meet the clinical requirements. The target area fitness and DVH of 3D-CRT were not so good as those of VMAT, which may be related to the field conditions of 3D-CRT. But the doses delivered to the spinal cord D1 and the infected lung (including V5, V30) in 3D-CRT were the lowest. But the average dose Dmean, V20 and V30 were higher compared with the other one plan. Furthermore, the average doses to contralateral lung, contralateral breast and heart were the lowest while the high dose point was higher. Because such field mode can maximally avoid the spinal cord, but lead to increasing the high dose area and the average dose of ipsilateral lung. IMRT also has good dose distribution in the target. It can reduce the maximum dose of the target area, and allow the average dose Dmean of target area to be closer to the prescribed dose. The target area fitness and DVH can meet the clinical needs. But its reception amount of the spinal cord D1 is higher than that in 3D-CRT and VMAT plans and the reception amount of ipsilateral lung (including V20, V30, the average dose Dmean) is the lowest. But the V5 and V10 are between 3D-CRT and VMAT plans. Also, the average doses to the contralateral lung, contralateral breast and the heart are between 3D-CRT and VMAT plans. The target area fitness and DVH of VMAT are better than the other plan. and the reception amount of the spinal cord D1 is between the other two plans. All indicators of ipsilateral lung were higher than that of other plans, and some other indicators (Dmean, V5) of contralateral lung, contralateral breast and heart are higher than the other plans. In addition, the indicator (V10) is better than the other plan. This study showed that VMAT has incomparable advantages than 3D-CRT plan in dose distribution and uniformity. They can guarantee the treatment target to obtain sufficient dose, reducing the cold and hot points of the dose in the target area. For the high dose region volume of the normal tissue, VMAT plans are smaller, while 3D-CRT is larger; For the low dose region volume of normal tissue, VMAT plans are larger, and 3D-CRT plan is smaller. The reason of having larger low dose volume of normal tissues in VMAT plans may be the following: field scattering radiation is more and field passes through the normal tissue. In general, the results shows that the ipsilateral lung V20 of the three plans are not significantly different. VMAT plan can significantly reduce the high dose volume of the ipsilateral lung (V30). But due to the increasing of scattered radiation, IMRT and VMAT plan also

significantly increase the low dose irradiated volume (V5, V10) compared to 3D-CRT plan. VMAT plan has more average dose to the contralateral lung, contralateral breast and heart than 3D-CRT plans. But we still cannot definitely tell the advantages and disadvantages of the two plans on lung protection. The is because the DVH parameters can be related to the radiation injury based on different angles. According to DVH data of the radiotherapy for lung cancer patients, the risk of radiation pneumonitis is related to the average dose of lung (MLD) and V20, V30 [10-12]. And V5, V10 are to the effective factors to estimate the occurrence of radiation pneumonitis [13]. This paper demonstrates VMAT plan protects the normal tissue of the affected side with good effect. VMAT Plans, it takes longer time than that of 3D-CRT because the parameters are adjusted and optimized repeatedly. Especially in the VMAT plan, the optimization process is divided into 5 steps, one by one completed. It not only needs to optimize the sub field and weight, but also because of many physical parameters in optimization plan, the optimization process is complex limited to the version of the system. The time-consuming process can reduce our work efficiency considerably.

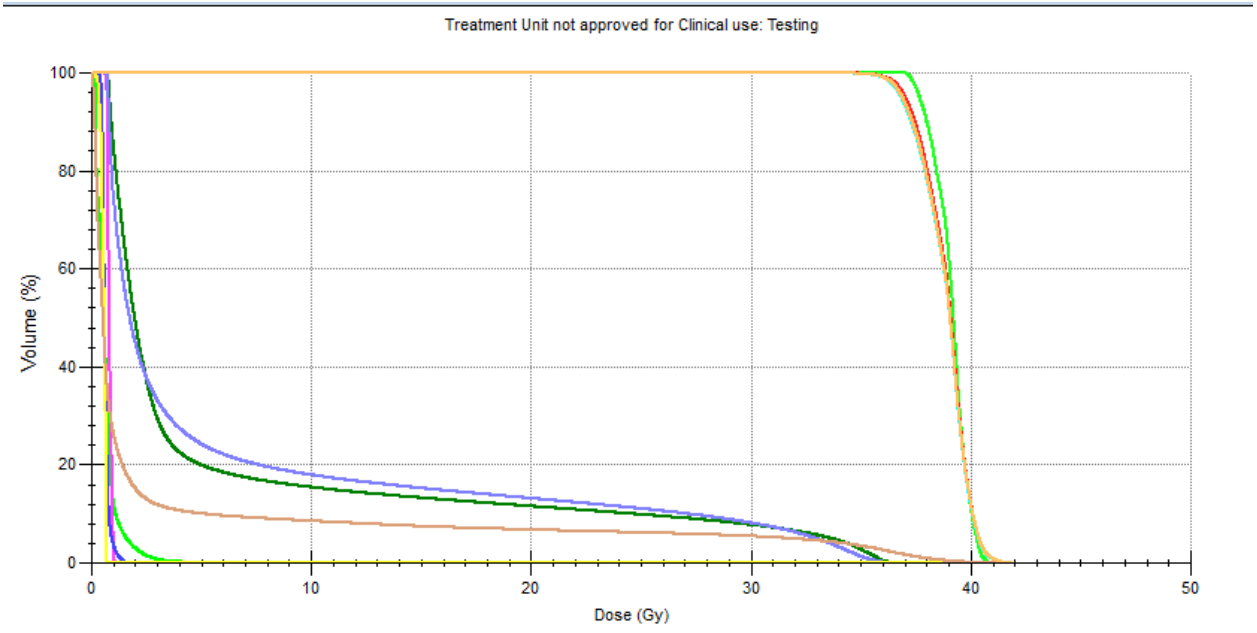

Fig. 1. 3D-CRT DVH for breast cancer patient

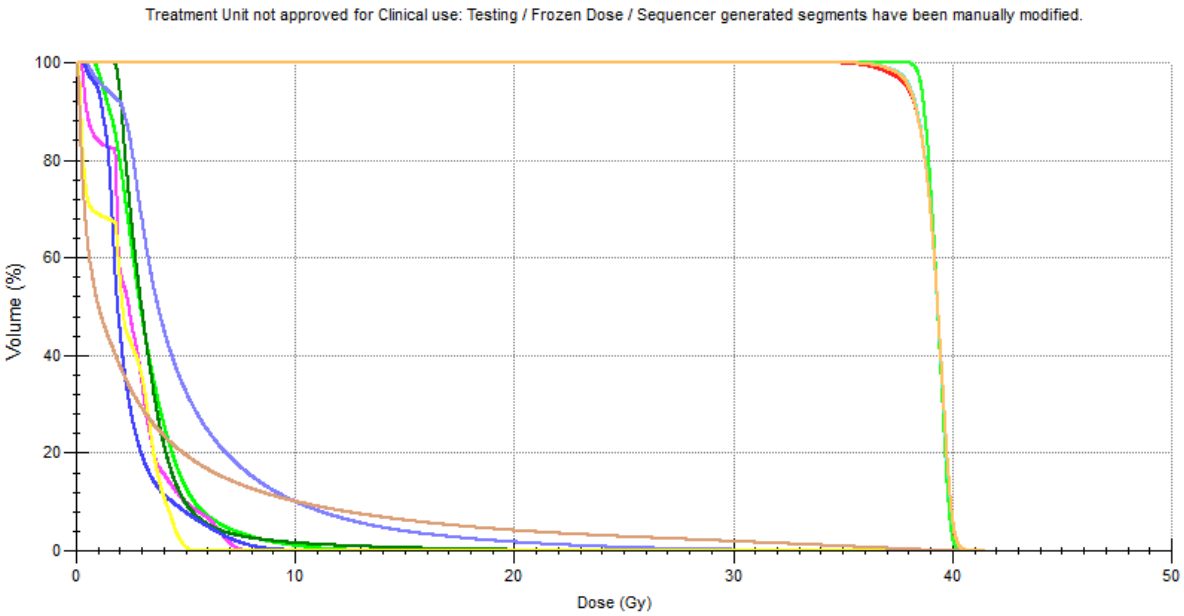

Fig. 2. VMAT DVH for breast cancer patient

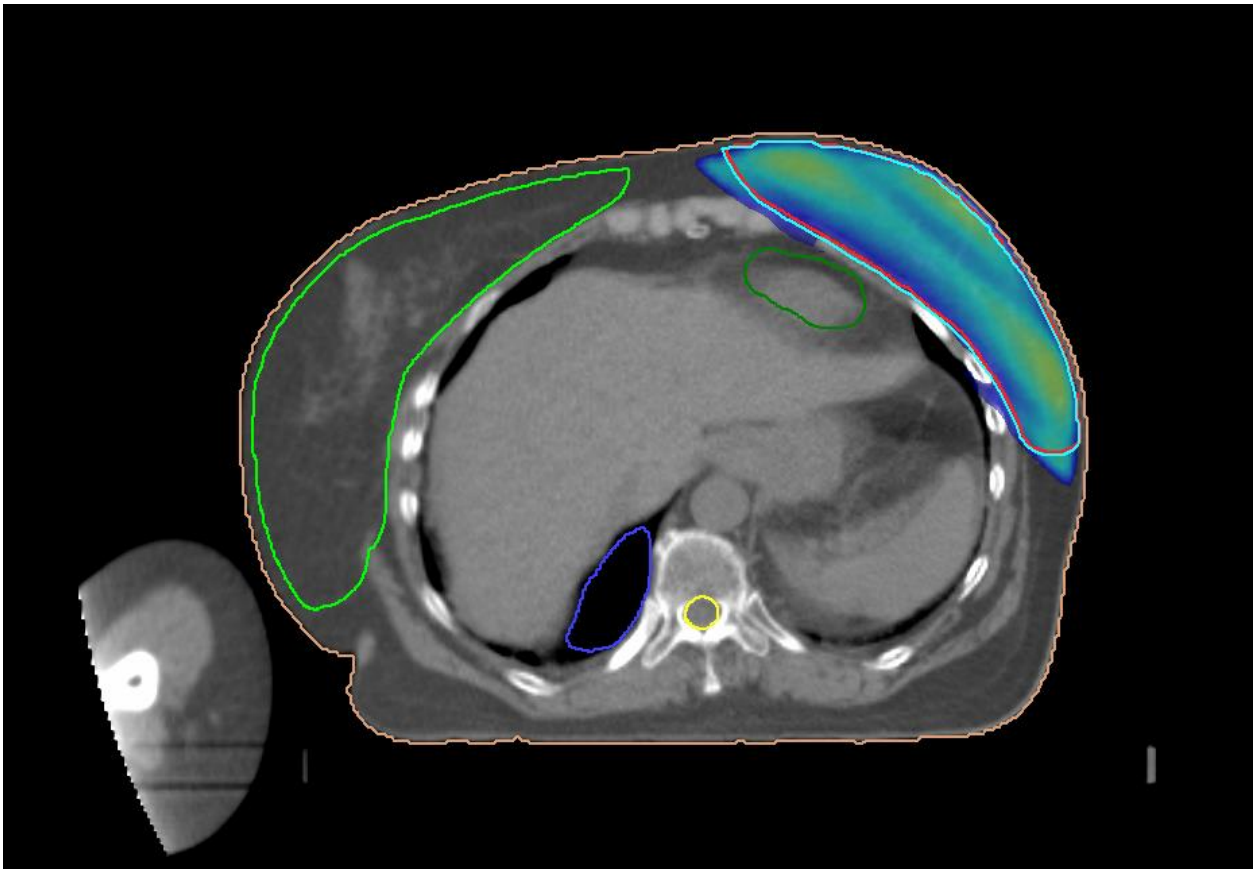

Fig. 3. 3D-CRT distribution

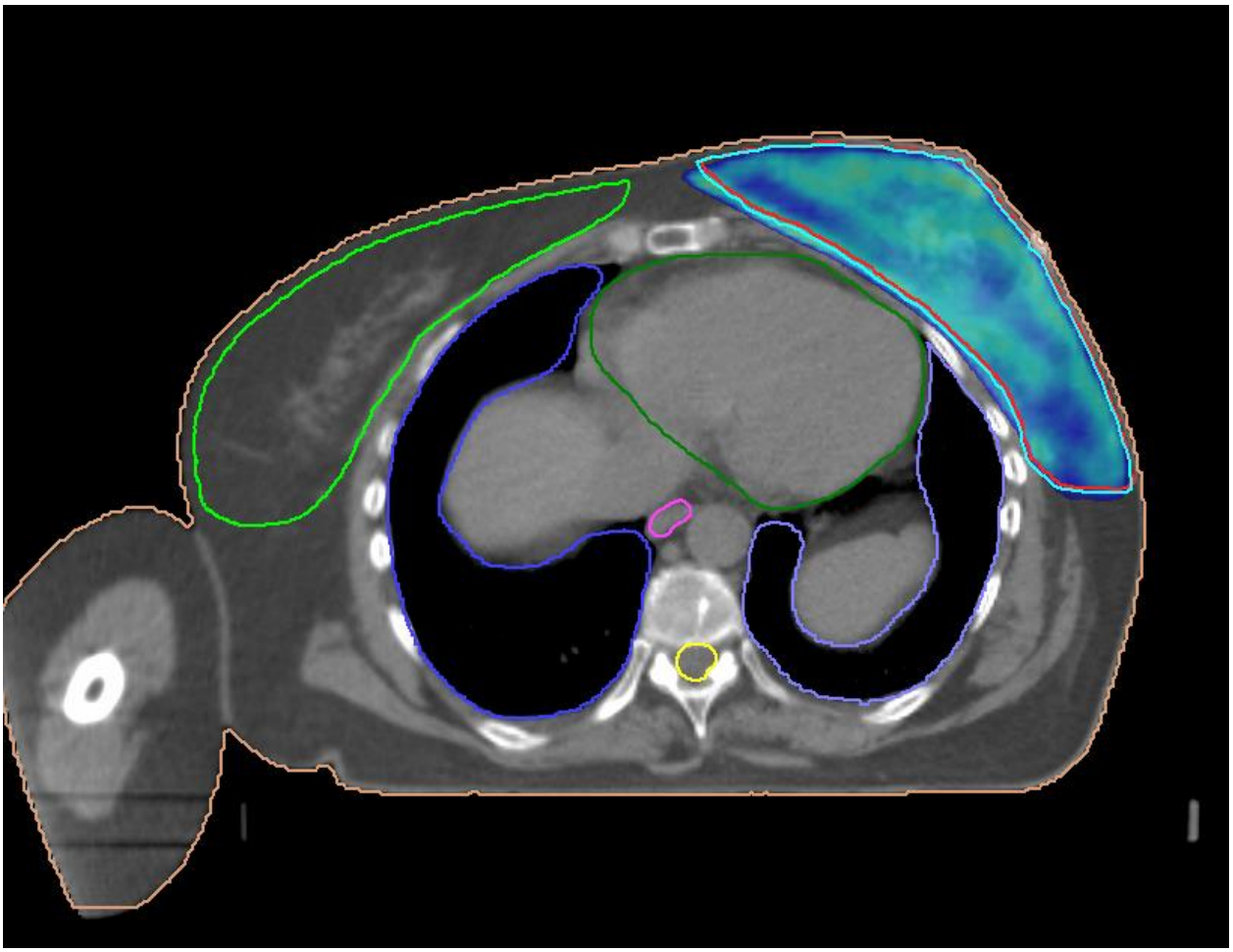

Fig. 4. VMAT distribution

Technique	VMAT	3D-CRT
Left Lung volume-20	1,71	13
Heterogenity Index CTV (volum95%)	36.8	36,8
Mean dose of Heart	3,4	5,9
Max dose of contra breast	20	16,7

Table 1. The mean doses in Gy

4. CONCLUSION

In our paper, we note that all of the three plans based on 3D-CRT and VMAT technology can achieve the basic requirements of clinical treatment, but in the process of treatment there are many uncertain factors. Therefore, we need to obtain an accurate

target volume delineation and strict control in order to assure a high quality. The dosimetric parameters pertaining to the VMAR have certain advantages. In addition, they have greatly increased the number of MU, the efficiency of treatment and time. But they need to further reduce the amount of the subject in the contralateral lung, heart, spinal cord, and the other organs.

REFERENCES

[1] Palma D., Vollans E., James K., et al., Volumetric Modulated Arc Therapy for Delivery of Prostate Radiotherapy: Comparison With Intensity-Modulated Radiotherapy and Three-Dimensional Conformal Radiotherapy. International Journal of Radiation Oncology Biology Physics, 2008, 72(4), 996-1001. doi:10.1016/j.ijrobp.2008.02.047.

[2] Vicini, F. A., Yan D., and Matter R. C., Intensity modulation to improve dose uniformity with tangential breast radiotherapy: initial clinical experience. International Journal of Radiation Oncology Biology Physics, 2000, 48(5), 1559-1568(10). doi.org/10.1016/S0360-3016(00)01396-1.

[3] Otto, K., Volumetric modulated arc therapy: IMRT in a single gantry arc. Medical Physics, 2008, 35(1), 310-317. doi.org/10.1118/1.2818738.

[4] Prescribing, Recording, and Reporting Photon-Beam Intensity-Modulated Radiation Therapy (IMRT): Contents. Journal of the Icru, 2010, 10(1), 1-106. doi.org/10.1093/jicru/ndq002.

[5] Yin Y., Chen J., Xing L., et al., Applications of IMAT in cervical esophageal cancer radiotherapy: a comparison with fixed-field IMRT in dosimetry and implementation. Journal of Applied Clinical Medical Physics, 2011, 12(12), 48-57. doi: 10.1120/jacmp.v12i2.3343.

[6] Li J. B., Wang J. G., Lu J., et al., [Influence of active breathing control on the dose distribution in the target of forward whole-breast intensity-modulated radiotherapy after breast conserving surgery]. Zhonghua zhong liu za zhi [Chinese journal of oncology], 2009. 31(8), 617-621. doi: 10.3389/fonc.2018.00087.

[7] Jagsi R., Jm B. D. M., Marsh R. B., et al., Unacceptable Cosmesis in a Protocol Investigating Intensity-Modulated Radiotherapy With Active Breathing Control for

Accelerated Partial-Breast Irradiation. International Journal of Radiation Oncology Biology Physics, 2010. 76(1), 71-78. doi: 10.1016/j.ijrobp.2009.01.041.

[8] Shaffer, R., Nichol A. M., and Vollans E., A comparison of volumetric modulated arc therapy and conventional intensity-modulated radiotherapy for frontal and temporal high-grade gliomas. International Journal of Radiation Oncology Biology Physics, 2009. 76(4), 1177-1184. doi: 10.1016/j.ijrobp.2009.03.013.

[9] Chen Jinhu, Y. Y., Liu Tonghai, Comparative study of radiotherapy planning for cervical esophageal cancer patients between fixed gantry intensity modulated radiation and RapidArc. Chinese Journal of radiation oncology, 2010, 19(5),429-433. DOI: 10.1120/jacmp.v12i2.3343.

[10] Ma Changsheng, Y. Y., Liu Tonghai, Dosimetric comparison between RapidArc and fixed gantry intensity modulated radiation of liver carcinoma. Chinese Journal of radiation medicine and protection, 2010, 30(5), 581-584. DOI: 10.1016/j.meddos.2010.12.001.

[11] Hernando M. L., Marks L. B., Bentel G. C., et al., Radiation-induced pulmonary toxicity: a dose-volume histogram analysis in 201 patients with lung cancer. International Journal of Radiation Oncology biology physics, 2001, 51(3), 650-659.

[12] Kwa S. L. S., Lebesque J. V., Theuws J. C. M., et al., Radiation pneumonitis as a function of mean lung dose: an analysis of pooled data of 540 patients. International Journal of Radiation Oncology biology physics, 1998, 42(1), 1-9. DOI: https://doi.org/10.1016/S0360-3016(98)00196-5.

[13] Fu Heyi, L.B., Xu Bingqing, Prospective clinical study of V5 and V10 in predicting radiation-induced lung injury and three dimensional conformal radiation therapy for non small cell lung cancer in stage III and IV. Chinese Journal of radiation oncology, 2009, 18(6), 439-442. doi: 10.3390/cancers10070222.

[14] Qiu, J.J., Chang Z., Wu Q. J., et al., Impact of Volumetric Modulated Arc Therapy Technique on Treatment With Partial Breast Irradiation. International Journal of Radiation Oncology Biology Physics, 2010, 78(1), 288-296. DOI: 10.1016/j.ijrobp.2009.10.036.

[15] Shaitelman S. F., Kim L. H., Yan D., et al., Continuous arc rotation of the couch therapy for the delivery of accelerated partial breast irradiation: a treatment planning

analysis. International Journal of Radiation Oncology Biology Physics, 2011, 80(3), 771-778. doi: 10.5306/wjco.v7.i5.370.

[16] Sun Tao, L. J., Xu Min, Dosimetric comparison of 3D-CRT, dIMRT, and RapidArc technology in partial external irradiation of breast. Chinese Journal of radiation medicine and protection, 2012, 32(1), 74-79. DOI: 10.7785/tcrt.2012.500174.

FREQUENCY DEPENDENCE OF MULTIPATH FADING OVER THE SEA UNDER DUCTING: REFRACTIVITY PROFILES PARAMETERS AND SEA SURFACE ROUGHNESS INFLUENCE (selected from CEMA'19 Conference)

I. Sirkova*

*Laser Radars Lab, Institute of electronics, Bulgarian Academy of Sciences

Tzarigradsko chaussee 72, 1784 Sofia, Bulgaria

Email : irina@ie.bas.bg

Abstract

Over water microwave propagation is often affected by the presence of evaporation duct. The tropospheric ducting is one of the major causes for multipath propagation. The ducting propagation mechanism is known to be highly frequency dependent whereas the prediction methods for multipath fading distribution suggest a rather slight dependence on frequency. In order to check this discrepancy, the paper studies the influence of the variations of important parameters of the evaporation duct log-linear refractivity profile and the sea surface roughness on the frequency dependency of multipath fading. The refractivity profiles serve as input to the parabolic equation method which provides a full-wave solution to the path loss problem. The sea surface roughness is modelled through two roughness reduction factors, one of them accounting for the shadowing. Ten frequencies of microwave range are used in four hypothetical over the sea links. The results are presented in form of path loss standard deviation versus frequencies for fixed ranges.

1. INTRODUCTION

The propagation conditions in coastal and maritime regions are often complicated by changes in the tropospheric refractive index leading to formation of tropospheric ducts [1]. This peculiarity makes the preliminary assessment of microwave propagation in those regions difficult and subject to significant errors. One of the consequences of the ducts' formation is the multipath propagation and, accordingly, the multipath fading [2, 3]. The assessment of fading is an important part of performance predicting of radio communication links. To achieve the necessary accuracy in performance predicting, sophisticated propagation channel modelling methods are applied which account

simultaneously for terrain irregularities, clear air propagation mechanisms, and antenna patterns. Among them the Parabolic Equation (PE) method [4] has become one of the most widely used to solve microwave propagation problems especially in complicated environments such as tropospheric ducting [4, 5]. Despite the variability of the marine boundary layer [6], for practical purposes one usually assumes lateral homogeneity for the refractivity and applies a single profile, approximated to account for the average behavior of the modified refractivity *M(z)* with height *z*, as environmental input to the PE. Special attention is paid to the modelling of *M(z)* for evaporation duct due to its frequent occurrence and particular importance in coastal and maritime regions. Most often the evaporation duct is modelled by log-linear height profile of the modified refractivity *M* [7]:

$$M(z) = M_0 + c_0\left[z - z_d \ln\left(\frac{z + z_0}{z_0}\right)\right] \quad (1)$$

where $M_0 = M(z = 0)$, z_0 is the aerodynamic roughness parameter usually taken to be 1.5 × 10−4 m [4], zd is the duct height corresponding to the height at which d*M*/dz = 0, c_0 is the critical potential refractivity gradient [8] usually taken to be 0.13. The physics behind this profile, based on the Monin–Obukhov similarity theory, is explained in [4, 7]. With above values of parameters c_0 and z_0, (1) has been obtained assuming thermally neutral troposphere stratification and does not account for the stability effects on the M profile. This most usual form of evaporation duct log-linear *M* profile is governed by one parameter - the duct height, z_d, which determines the other important duct parameter, the *M*-deficit, $\Delta M = M(z_d) - M_0$. Recently, attempts at improving (1) have been made by changing the slope in different parts of the log-linear curve [8, 9], thus making it to better fit the experimental profiles and, hence, include the influence of tropospheric stability. In [8] the parameters of evaporation duct refractivity model (1) have been optimized using radiosonde data. This study has shown that the best log-linear model formulation would include, except for the most important duct parameter z_d, also duct curvature and mixed layer slope (mixed layer is the well-mixed by turbulent mixing layer above the duct). In (1) c_0 and z_0 are parameters responsible for the profile curvature (c_0 changes the radius of curvature surrounding the duct whereas z_0 changes the curvature below the duct only [8]). Those parameters influence also the *M*-deficit under the same z_d.

The ducting propagation mechanism is highly frequency dependent whereas the prediction methods for multipath fading distribution on line-of-sight links suggest a rather slight dependence on frequency [2, 10]. In order to check this discrepancy, this work studies how the parameters of profile (1) and the sea surface roughness reflect on the frequency dependency of (large-scale) multipath fading in the case of microwave propagation over the sea under evaporation duct conditions. The evaporation duct model (1), with varying parameters z_d and c_0, serves as input to the PE method [4] to compute the path loss' standard deviation in the areas of interests. Ten frequencies of microwave range are used in four hypothetical over the sea line-of-site links. On the basis of the "effective" reflection coefficient concept [4], the sea surface roughness is modelled through two roughness reduction factors (RRFs): the original Ament's roughness reduction factor [11] and modified Ament's RRF with shadowing effect included as proposed in [12] and implemented for ducting propagation in [13].

2. DESCRIPTION OF THE METHOD

The PE method is applied as implemented in "Advanced propagation model (APM) Computer software configuration item (CSCI) documents", Space and Naval Warfare Systems Center Tech. Doc. 3145, San Diego, CA, 2002. Those routines make use essentially of the 2D narrow-angle forward-scatter scalar PE, (2), which provides a full-wave solution to the path loss problem:

$$\frac{\partial u(x,z)}{\partial x} = \frac{i}{2k}\frac{\partial^2 u(x,z)}{\partial z^2} + \frac{ik}{2}\left(m^2(x,z)-1\right)u(x,z). \tag{2}$$

Details on the derivation of (2), its validation and use for electromagnetic (EM) field calculations under tropospheric ducting conditions are largely reported in the literature [4, 5] and will not be repeated here. In (2) k is the free-space wave number, $m = M \times 10^{-6}+1$ is the modified refractive index, $u(x,z)$ is a slow-varying along the preferred propagation direction, x, function related to the corresponding to the polarization transverse EM field component, x and z stay for range and altitude. The popularity of (2) is related to its easy numerical solution through marching algorithms. In addition to boundary conditions, (2) requires knowledge of initial field [4]. The main drawback of (2) is the neglect of backscattering. The studied microwave propagation problem is

characterized by EM field variations over scales much larger than the wavelength, grazing incident angles, and smooth variation of the tropospheric refractive index with *x*; under these conditions the forward-propagated field plays dominant role and this assures the applicability of (2).

The initial field required to start the calculations is provided by horizontally polarized Gaussian beam source with pattern factor given by (3) where θ_0 and θ_s are the half power beamwidth and the antenna elevation angle. Initially, smooth perfect conducting underlying surface (sea) is assumed. The results are presented in the form of standard deviation of the path loss (*PL* in dB, see (4)) in the area of interest versus frequency for fixed range.

$$F(\theta) = \exp\left[\frac{\ln(0.707)(\theta-\theta_s)^2}{\left(\theta_0/2\right)^2}\right], \tag{3}$$

$$PL = 20\log\left(\frac{4\pi r}{\lambda}\right) - PF,\ PF = 20\log|u(x,z)| + 10\log(r) + 10\log(\lambda). \tag{4}$$

In (4) λ is the free-space wavelength, *r* is the distance between the corresponding points, and *u*(*x*,*z*) is the solution of the PE (2).

The correct modelling of EM propagation over rough sea surface is still an open issue due to the difficulties in implementing all scattering mechanisms in the electromagnetic model. A practical approximate solution is to account for the surface roughness effects by defining an "effective" reflection coefficient R_{eff}, see (5) below, representing the Fresnel reflection coefficient from flat surface, R_{F}, multiplied by a RRF R_{rf} [4]. Two RRFs have been widely used in over-the-ocean microwave propagation: the Miller-Brown one [14] and Ament's RRF [11]. Comparisons of the propagation prediction results based on combination of these two RRFs with different propagation models to measurements' data do not allow concluding which of them is more accurate; a good discussion on this issue may be found in [15]. The propagation at very low grazing angles, typical for tropospheric ducting, is additionally complicated by shadowing effect due to sea surface waves [12, 15]. It is to be noted that both above mentioned RRFs affect only the magnitude of the complex Fresnel reflection coefficient and do not account for the shadowing. In order to go closer to the observed experimental results, theoretical

efforts have been made to improve the RRF's accuracy by introducing the shadowing effect [12, 15]. Equation (6) below presents the original Ament's roughness reduction coefficient R_A [11]. The R_{rf} from (7) is obtained in [12] using the same statistics (Gaussian statistics of sea surface heights and slopes) as the one assumed for the derivation of the original Ament's roughness reduction factor R_A. The R_{rf} from (7) accounts for the shadowing effect of the sea surface roughness by introducing a phase correction to R_A. In (6) and (7) k is the wave number in free space, φ is the plane wave grazing incidence angle to the rough surface, σ_ξ is the standard deviation of the surface height ξ, $\tilde{m}_\xi$ and $\tilde{\sigma}_\xi$ are the mean value and standard deviation of the illuminated surface heights only (see [12] for details), $Q=2k\sin(\varphi)$.

$$R_{eff} = R_{rf} R_F \quad , \tag{5}$$

$$R_A = \exp\left[-2k^2\sigma_\xi^2 \sin^2(\varphi)\right] \ , \tag{6}$$

$$R_{rf} = \exp\left(-jQ\tilde{m}_\xi - \frac{Q^2\tilde{\sigma}_\xi^2}{2}\right). \tag{7}$$

In this study the parameters σ_ξ, $\tilde{m}_\xi$, and $\tilde{\sigma}_\xi$ needed to compute (6) and (7) are taken for wind speed of 7 km/s, see [12, 13] for formulas and details.

3. RESULTS AND DISCUSSIONS

For every frequency the *PL* is calculated versus height for fixed ranges R = 20 km, R = 40 km for four hypothetical links: A) z_t = 40 m, $\theta_0 = 5^0$; B) z_t = 15 m, $\theta_0 = 5^0$; C) z_t = 40 m, $\theta_0 = 1^0$; D) z_t = 15 m, $\theta_0 = 1^0$, where z_t stays for the transmitter height. Three different values for c_0 are used: c_0 = 0.13, c_0 = 0.11 and c_0 = 0.19, the last two accounting for the deviation from the thermally neutral troposphere stratification. For all cases $\theta_s = 0^0$ in (3). The parameter z_0 is kept equal to 1.5×10^{-4} m in all reported examples. The receiver height is supposed to start from z_r = 5 m and go up to 150 m. This area of interest is divided in two parts: z_1 from 5 m to the top of evaporation layer, defined here as $z_L = 2z_d$, see [8], and z_2 which ranges from the evaporation layer height z_L up to 150 m. The frequencies are shown in Table 1. Those frequencies belong to the ranges used for coastal and maritime radars (lower ranges) and fixed and mobile links (upper ranges). The results are presented in form of *PL* standard deviation versus frequencies.

2.4	3.1	4.5	5.6	7.1	8.4	9.3	13.4	15.4	19.7

Table 1. Frequencies used, GHz

Fig. 1 shows range-independent duct with z_d = 35 m = ct over the entire distance of R = 20 km for link A) and the two areas of interest, z_1 and z_2. Fig. 2 reports similar results but for z_d = 10 m = ct and link B). On both figures one can see comparison for three different values of c_0. As it is seen from figs. 1, 2, the frequency dependency of *PL* standard deviation is rather slight and has similar character for the three values of c_0; it is higher in area z_1, especially for the lower frequencies, see Fig. 2a). This may be due to the fact that the lower frequencies are not well trapped in the

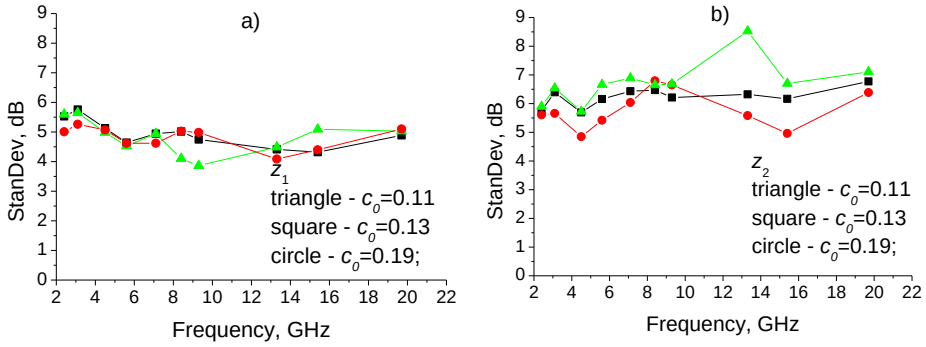

Fig. 1. Range-independent duct: z_d = 35 m, R = 20 km, link A).

thinner duct from Fig. 2. For the two figs. and area z_1, both z_t and z_r are submerged in the evaporation layer (z_t, z_r < z_L) which determines the more pronounced influence of the duct for area z_1 than for z_2.

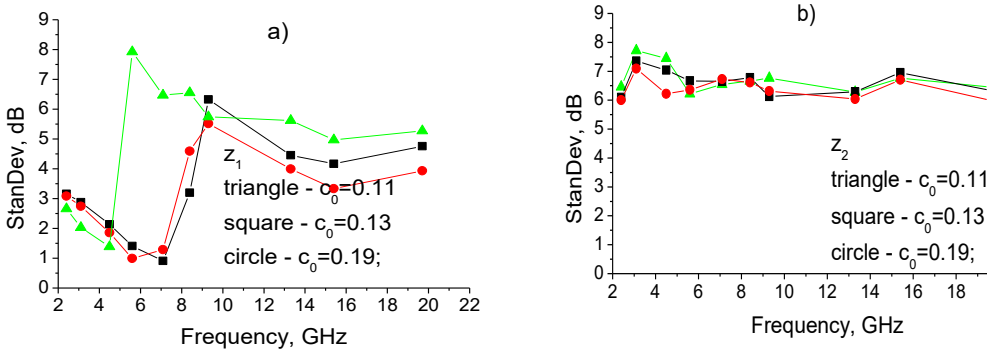

Fig. 2. Range-independent duct: zd = 10 m, R = 20 km, link B).

The frequency dependency of standard deviation for range-dependent duct in sense that the start refractivity profile has $c_0 = 0.13$ which changes to $c_0 = 0.19$ at the mid path has also been studied; the results (not reported here) indicated (once again) the rather week influence of the variation of c_0 (except for the lowest frequencies), especially in area z_2. Further, on fig. 3, another range-dependent case is demonstrated by changing the z_d parameter in the middle of the path from initial $z_d = 10$ m to $z_d = 15$ m, $c_0 = 0.19 = ct$, $R = 20$ km, link C). As expected, on Fig. 3 for the area z_1 the change in z_d almost does not reflect on the frequency dependency because z_t for link C) is above evaporation layer z_L for both z_d values. The influence of increased z_d is higher in the area z_2.

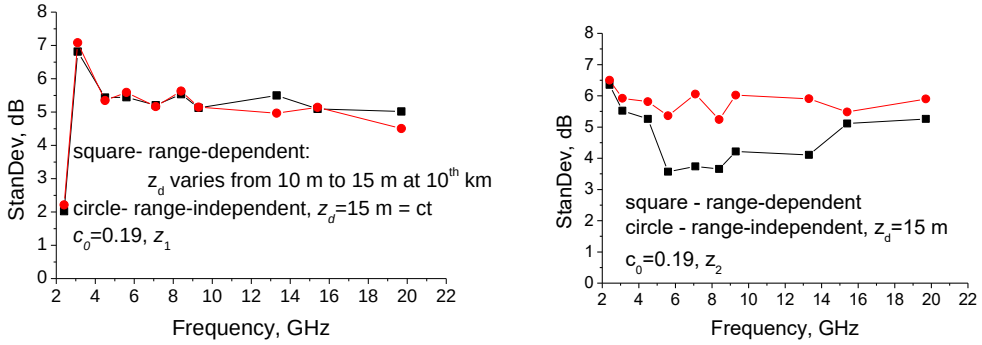

Fig. 3. Comparison between range-dependent and range independent duct, R = 20 km, link C).

On Figs. 4 – 7 results are shown for rough sea surface. Fig. 4 shows the influence of the roughness reduction factor R_A from (6) for original Ament roughness reduction coefficient: the introduction of R_A increases the frequency dependency and leads to reduction of the standard deviation values for higher frequencies both in z_1 and z_2 areas. Figs. 5-7 present comparison between smooth sea and rough sea modelled with R_A and R_{rf} from (7): Fig. 5 refers to link A) with $z_d = 15$ m, $R = 20$ km; Fig. 6 reports comparison between $c_0 = 0.11$ and $c_0 = 0.19$ for R_{rf} from (7) for link A) with $z_d = 15$ m, $R = 20$ km; fig. 7 refers to link C) with $z_d = 35$ m, $R = 40$ km. The roughness with application of shadowing, (7), increases the frequency dependency in comparison to smooth sea and in z_1 often has opposite trend to that of the roughness introduced through R_A. In z_2, for higher frequencies, the frequency dependency of *PL* standard deviation for R_{rf} from (7) follows that obtained for R_A but with higher values. In [13] it has been demonstrated that the introduction of the rough sea surface and, especially, of the roughness reduction

factor given by (7), destroys the (guiding) duct structure and reduces the long-range ducted propagation. The electromagnetic energy is scattered by the roughness and this reduces the fading depths for all links and distances. The higher the frequency, the higher the depths reduction. In area z_2 increases the difference in *PL* standard deviation frequency dependency between stable ($c_0 = 0.11$) and unstable ($c_0 = 0.19$) troposphere stratification, see Fig. 6.

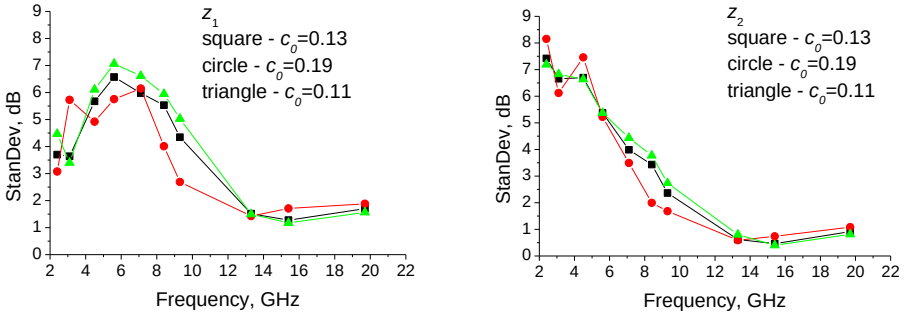

Fig. 4. Rough sea surface: RA from (6), zd = 35 m, R = 40 km, link C).

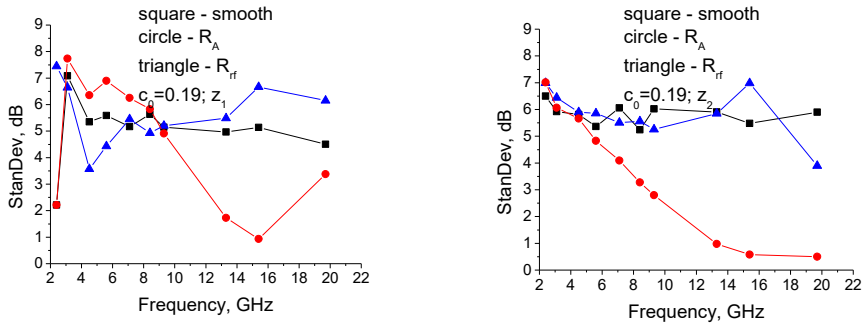

Fig. 5. Comparison between smooth sea, original Ament RA and Rrf, (7), link A), zd=15 m, R=20 km.

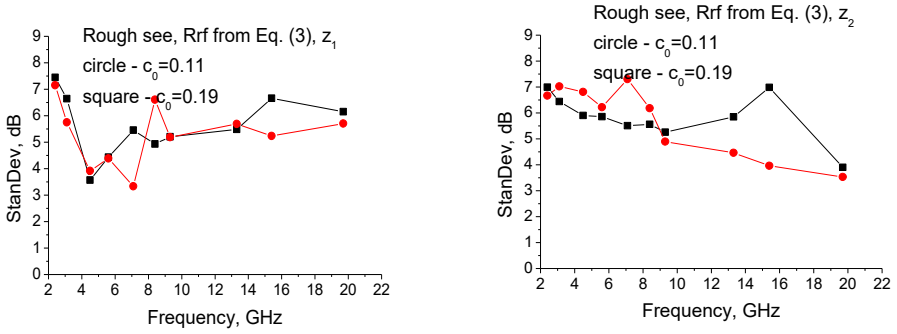

Fig. 6. Comparison between c0 = 0.11 and c0 = 0.19 for Rrf from (7), link A), zd=15 m, R=20 km.

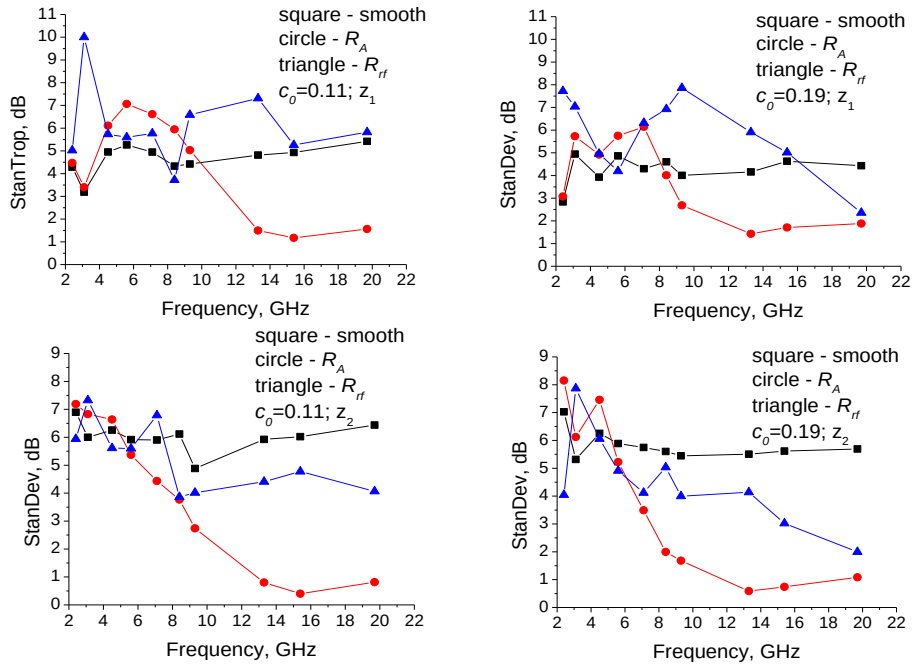

Fig. 7. Comparison between smooth sea, original Ament RA, and Rrf, (7), link C), zd=35 m, R=40 km.

4. CONCLUSION

On the basis of Figs. 1-7 (as well as other results not reported here) the following concluding remarks may be drawn:

1. For smooth sea - in the studied limits, the results support the applicability of profile (1) with $c_0 = 0.13$. In general, the frequency dependency of multipath fading under ducting conditions modelled by (1) for smooth sea surface is rather slight and appears to be in accordance with the slight influence of the frequency dependent factor in widely applied prediction methods [2, 10]. More attention is to be paid to lower frequencies when ducts with low z_d are present. The particular case when z_t is between z_d and evaporation layer z_L needs additional studies.

2. For rough sea - the roughness introduced through R_A increases the frequency dependency of the *PL* standard deviation in the same time decreasing its values for higher frequencies. The introduction of shadowing effect, (7), influences both z_1 and z_2 regions, it modifies the tendency of the original Ament's roughness reduction factor to reduce the values of *PL* standard deviation for higher frequencies. In further investigations more attention should be paid on the combined effect of different from neutral troposphere stratification and sea surface roughness. The reported results for sea surface roughness

influence on frequency dependent fading can not be assessed using traditional methods. More investigations with application of different RRFs and corrections for shadowing (and, possibly, attraction of additional scattering mechanisms as diffraction) as well as further comparisons to measurement data are needed in order to substantiate the reported results.

ACKNOWLEDGEMENT

This work was supported in part by the Ministry of Education and Science of Bulgaria under grant agreement № D01-151/2018.

REFERENCES

[1] ITU-R P.453-9, "The Radio Refractive Index: its Formula and Refractivity Data", 2003.

[2] R. L. Olsen, T. Tjelta, L. Martin, and B. Segal, "Worldwide techniques for predicting the multipath fading distribution on terrestrial LOS links: comparison with regional techniques," IEEE Trans, vol. AP-51, no. 1, pp. 23-30, 2003.

[3] S. R. Saunders, and A. Aragon-Zavala, Antennas and Propagation for Wireless Communication Systems, Chichester, West Sussex, UK: John Wiley & Sons, 2nd edition, 2007.

[4] M. Levy, Parabolic Equation Methods for Electromagnetic Wave Propagation, UK: IEE electromagnetic waves series 45, 2000.

[5] I. Sirkova, "Brief review on PE method application to propagation channel modeling in sea environment," Open Engineering, vol. 2, no. 1, pp. 19-38, 2012.

[6] B. W. Atkinson, and M. Zhu, "Coastal effects on radar propagation in atmospheric ducting conditions," Meteorological Applications, vol. 13, pp. 53–62, 2006.

[7] R. A. Paulus, "Practical application of an evaporation duct model," Radio Science, vol. 20, pp. 887–896, 1985.

[8] J. T. Saeger, N. G. Grimes, H. E. Rickard, and E. E. Hackett, "Evaluation of simplified evaporation duct refractivity models for inversion problems," Radio Science, vol. 50, no. 10, pp. 1110–1130, 2015.

[9] J.-P. Zhang, Z.-S. Wu, Q.-L. Zhu, and B. Wang, “A four-parameter M-profile model for the evaporation duct estimation from radar clutter,” Progress In Electromagnetics Research, vol. 114, pp. 353-368, 2011.

[10] ITU-R P.530-9, “Propagation Data and Prediction Methods Required for the Design of Terrestrial Line-of-Sight Systems”, 2001.

[11] W. S. Ament, "Toward a theory of reflection by a rough surface," Proc. IRE, vol. 41, no. 1, pp. 142–146, 1953.

[12] V. Fabbro, C. Bourlier, and P.F. Combes, "Forward propagation modeling above Gaussian rough surfaces by the parabolic wave equation: introduction of the shadowing effect," Progress In Electromagnetics Research, vol. 58, pp. 243–269, 2006.

[13] I. Sirkova, "Propagation factor and path loss simulation results for two rough surface reflection coefficients applied to the microwave ducting propagation over the sea," Progress In Electromagnetics Research M, vol. 17, pp. 151–166, 2011.

[14] A. R. Miller, R. M. Brown, and E. Vegh, "New derivation for the rough surface reflection coefficient and for the distribution of sea-wave elevations," IEE Proc.-H, vol. 131, pp. 114–116, 1984.

[15] D. E. Freund, N. E. Woods, H.-CH. Ku, and R.S. Awadallah, "The effects of shadowing on modeling forward radar propagation over a rough sea surface," Waves in Random and Complex Media, vol. 18, no. 3, pp. 387–408, 2008.

ON THE ANALYSIS OF SEA SURFACE IMAGES RELATED TO SEA STATE DETERMINATION BY MULTIFRACTAL METHODS (selected from CEMA'19 Conference)

N. Ampilova[*], I. Soloviev[*], A. Kotopoulis[**], G. Pouraimis[**] and P. Frangos[**]

[*] St. Petersburg State University, Comp. Sci. Dept.,

St. Petersburg, Russia

Email: n.ampilova@spbu.ru, i.soloviev@spbu.ru

[**] School of Electrical and Computer Engineering,

National Technical University of Athens, Greece

Email: pfrangos@central.ntua.gr

Abstract

Digital images may register states of a process, and image analysis help us to study this process and its peculiarities. In spite of the fact that there are a lot of textbooks on techniques of image analysis, any new problem may require a new method. Last decades fractal and multifractal methods are often used to analyze high resolution images having complex textures. In many cases fractal characteristics may be considered as classifying signs for further clustering. In this paper we present two multifractal methods. The first method allows us to obtain multifractal spectra and decompose an initial image into the union of nonintersecting sets. The second one is based on the transformation of an initial measure distribution under so called "direct multifractal transform" and calculation of information dimensions of measure supports. The examples of application of these techniques are given for various kinds of sea surface images.

1. INTRODUCTION

Now the methods of fractal and multifractal analysis are widely used to analyze images with complex structure. Such images are often fractals or multifractals. Fractal sets have a self-similarity property and may be described one numerical characteristic — fractal dimension. Multifractal sets are unions of several fractal subsets, which of them has its own fractal dimension, being these subsets are arranged in a complex intertwined manner. Hence a common characteristic for multifractals is multifractal spectrum — the set of fractal dimensions of its subsets. Our experience in analyzing biomedical preparation images (in [1] we calculated Rényi spectra for images of pharmacological

solutions of Ag, and in [2, 3] we applied such methods for sensitive crystallization images) testifies that the good separation of spectra results in successful classification of similar images.

In this work we consider two methods for calculation of multifractal characteristics for digital images: a method based on calculation so called density function, which is calculated for each pixel and characterizes intensity changes in its neighbourhood, and calculation of the set of information dimensions both for a given spectrum and its modified variants which are obtained by a renormalization of a given measure. Additionally, in this method we calculate the spectrum of averaged exponents of singularity. Thus, to characterize an image we have 2 spectra. The combination of two methods increases the possibility for classification of images.

2. MULTIFRACTAL SPECTRUM BY USING DENSITY FUNCTION

We consider a special density function [4] to calculate the singularity power for every pixel. Then we combine all the pixels with close values of density function, which results in partition of the image on the subsets — so called level sets. For each level set we calculate its fractal dimension.

Let μ be a measure defined through pixel intensities for a given digital image. For $x \in R^2$ we denote $B(x,r)$ a square of length r with center x. Let $\mu\big(B(x,r)\big) = kr^{d(x)}(x)$, where $d(x)$ is so called local density function of x, and k some constant. Taking several values for r we have

$$d(x) = \lim_{r \to 0} \frac{\log \mu(B(x,r))}{\log r} \qquad (1)$$

The density function measures the non-uniformity of the intensity distribution in the square $B(x,r)$. The set of all points x with local density α is a level set $E_\alpha = \{x \in R^2 : d(x) = \alpha\}$. In practice, not to increase the number of level sets, one really consider the sets $E(\alpha, \varepsilon) = \{x \in R^2 : d(x) \in [\alpha, \alpha + \varepsilon)\}$, where ε is a real number.

The set of fractal dimensions of E_α is the multifractal spectrum $f(\alpha)$.

3. MULTIFRACTAL SPECTRUM BY USING STATISTICAL SUM

It is usually assumed that an image is partitioned by cells with size l, the number of cells is N(l) and the measure of i-th cell is $p_i(l) \sim l^{\alpha_i}$. Consider the statistical sum $S(q,l) = \sum_{i=1}^{N(l)} p_i^q(l))$ (called also the sum of moments of the measure), where q is a real number, and the sequence of measures $\mu(q,l) = \{\mu_i(q,l)\}$ generated from the initial measure by the direct multifractal transform $\mu_i(q,l) = \frac{p_i^q(l)}{\sum_{i=1}^{N} p_i^q(l)}$. The method proposed in [5] is based on the calculation of information dimension of a measure support M by the formula

$$dim\, M = -\lim_{N\to\infty} \frac{\sum_{i=1}^{N} p_i \ln p_i}{\ln N} \tag{2}$$

The direct multifractal transform recalculates the initial measure by using statistical sum, and hence it depends on q as well. For any measure from the generated sequence one may calculate the singularity power averaged over the measure and the fractal dimension of the support of the measure corresponding to this singularity power. Hence we obtain the averaged singularity spectrum $\alpha(q)$, and the fractal dimension of the support of the measure $f(q)$ as functions of the parameter q. Eliminating q one can obtain the relation between singularity values and fractal dimensions of corresponding subset.

For each measure $\mu(q,l)$ one can calculate information dimension of its support. As q changes, we have a set $f(q)$ of information dimensions of $\mu(q,l)$ supports, where

$$f(q) = \lim_{l\to 0} \frac{\sum_{i=1}^{N} \mu_i(q,l) \ln \mu_i(q,l)}{\ln l} = \lim_{l\to 0} \frac{f(q,l)}{\ln l} \tag{3}$$

We also calculate averaging exponents over the measure $\mu(q,l)$, i.e.

$$\sum_{i=1}^{N} \alpha_i \mu_i(q,l) = \frac{\sum_{i=1}^{N} \ln p_i(l) \mu_i(q,l)}{\ln l} = \frac{\alpha(q,l)}{\ln l} \tag{4}$$

and then the limit $\alpha(q)$ of these averagings when $l \to 0$. Hence, we obtain

$$\alpha(q) = \lim_{l\to 0} \frac{\alpha(q,l)}{\ln l} \tag{5}$$

Such a method allows us to obtain the set of dimensions $f(q)$ and the set of averaging exponents $\alpha(q)$ as functions of the parameter q.

In practice, to obtain the above values we should do the following. For every q we take several values of variable l, calculate sets of points $(\ln l, f(q,l))$ and $(\ln l, \alpha(q,l))$ respectively. Then, by using the least square method, we find the corresponding straight

lines (in double logarithmic scale), and their tangent coefficients give us the approximate values of $f(q)$ and $\alpha(q)$ respectively. Thus, we have the set of information dimensions of the supports of the measures obtained from the initial measure by the direct multifractal transform. In [6] we applied this method to analyze biomedical preparation images, and in [7] it was used to study crystallization images.

4. NUMERICAL EXPERIMENTS

4.1 Density function method - Grayscale

Fig. 1. Optical images of sea surface related to sea state determination: calm sea surface (left) and disturbed sea surface (right).

Values of density function lie in diapason [1.73,2.23] for calm, and [1.52,2.42] for disturbed sea. We note that wider interval corresponds to more complex structure of the image. Level sets were constructed with step 0.1. The graphs of multifractal spectra are given in Fig. 2, below.

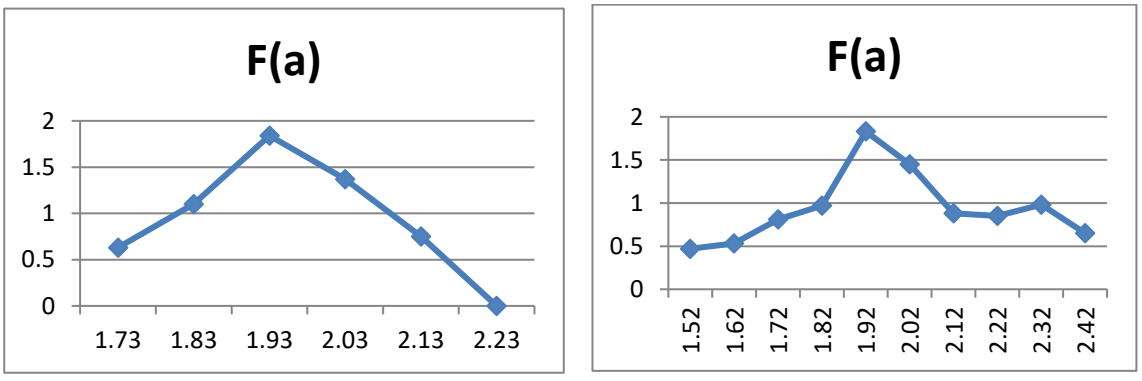

Fig. 2. Multifractal spectrum for calm sea surface (left) and disturbed sea surface (right). The images are represented in grayscale.

Level sets for image of calm sea are shown in Fig. 3, below. These sets illustrate a decomposition of an image on nonintersecting subsets. Each subset contains pixels having density function value in an interval $[a, a + 0.1)$, where $a = 1.73,1.83,193,2.03,2.13$. Thus, the number of subsets shown equals the number of intervals between values of $d(x)$ on OX axis. The corresponding graph shows values of fractal dimensions of these sets. We see that image (c) has the most intensive density, and on the graph we see that this subset has the maximal fractal dimension.

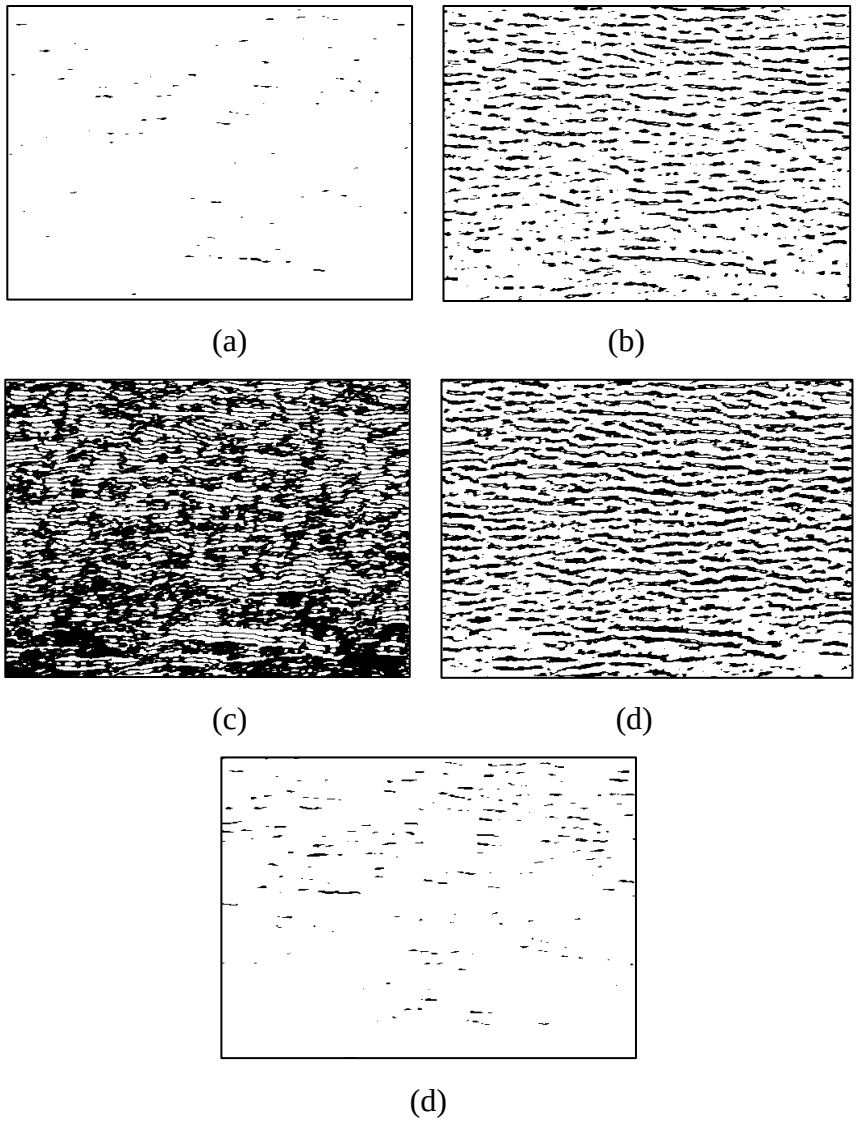

Fig. 3. Level sets for calm sea image: the decomposition of the image on nonintersecting subsets.

4.2 Density function method - Blue component of RGB

Calculation of density function values for images of calm and disturbed sea surface presented in Blue component of RGB led to the following results. The interval of density function values for calm sea is [1.9,2.09], for disturbed sea is [1.7,2.28]. We see that the first interval is rather narrow, which means that intensities of pixels change a little, and the image has more uniform structure, whereas for the disturbed sea the more complex structure is revealed. Level sets were constructed with step 0.05. Graphs of multifractal spectra for images in blue component are given on Fig. 4.

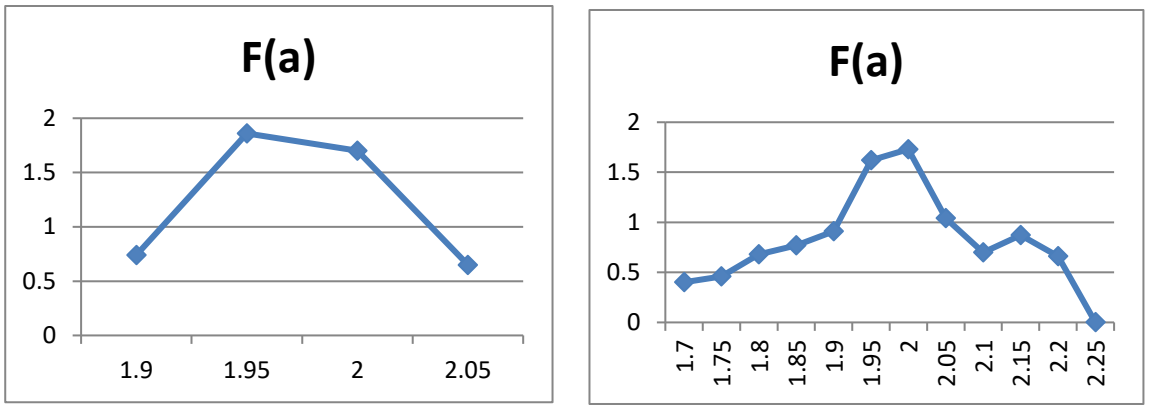

Fig. 4. Multifractal spectra for calm (left) and disturbed (right) sea surface. The images are represented in Blue component of RGB.

4.3. Method using generalized statistical sum - Grayscale

The application of the second method results in the graphs shown on Fig. 5.

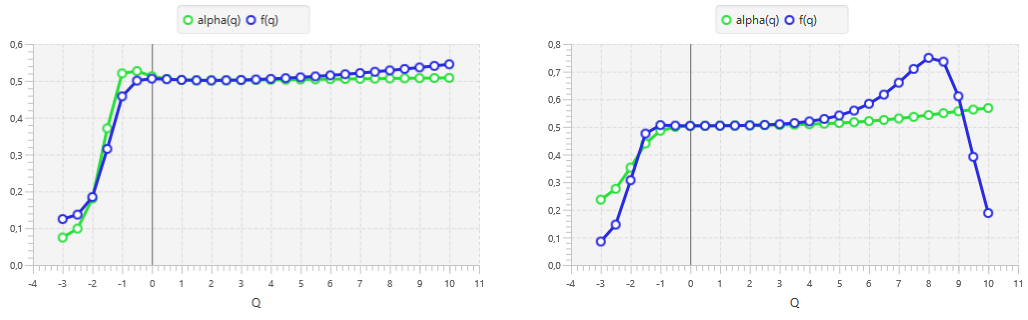

Fig. 5. Graphs of singularity and information dimensions for calm sea (left) and disturbed sea (right) in grayscale.

4.4 Method using generalized statistical sum - Blue component

We performed calculations for the representation of images in blue component. The results are shown on Fig. 6. We see that graphs are different independent of color representation.

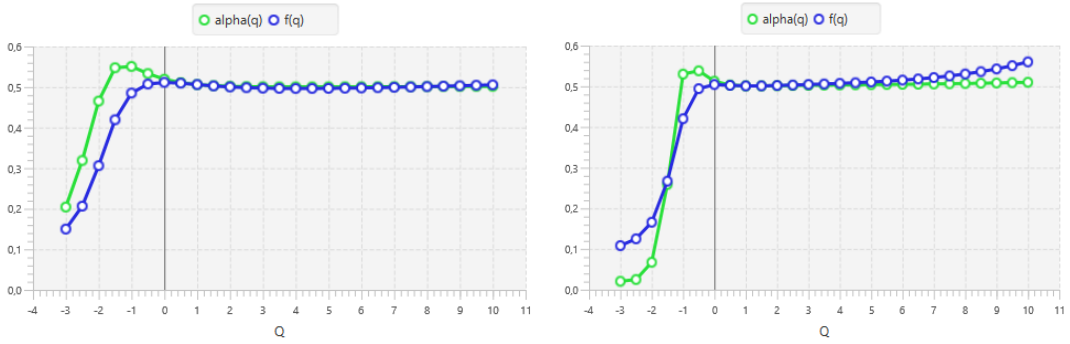

Figure 6. Graphs of singularity and information dimensions for calm sea (left) and disturbed sea (right) in Blue component.

5. CONCLUSION

The results of numerical experiments show that the methods applied may be useful for analysis of sea surface images and sea state determination, since graphs of multifractal spectra look quite different for different types of sea surfaces. It should be noted that we observe it in various color representation. The methods are rather perspective for analysis of images having complex structure such as images considered to determine sea state.

ACKNOWLEDGEMENT

Three (3) of the authors (A. Kotopoulis, G. Pouraimis and P. Frangos) would like to thank FFI Institute of Oslo, Norway, for the two (2) optical images of the sea surface, related to sea state determination (images obtained by FFI during 'NEMO 2014' trials in Taranto, Italy, September 2014). Furthermore, the authors acknowledge the support by the 'International Mobility Program', National Technical University of Athens (NTUA), Greece, which facilitated the scientific collaboration between the authors of this paper in the area of 'fractal techniques'.

REFERENCES

[1] E. Gurevich, N. Ampilova, I. Soloviev. "On a natural-science investigation of the ultralow doses effect", Proc. 8 Int. Conf. CEMA13, 17-19 Oct. 2013, Sofia, Bulgaria. p. 85-88.

[2] N. Ampilova, I. Soloviev. "Fractal analysis methods in investigation of low doses effects", Proc. 12 Int. Conf. CEMA17, 12-14 Oct. 2017, Sofia, Bulgaria, p. 10-14.

[3] N. Ampilova, E. Kulikov, V. Sergeev, I. Soloviev. "Fractal analysis methods in investigation of biomedical preparations images". Differential equations and control processes, 1, 2018, p. 109-125, http://www.math.spbu.ru/diffjournal/pdf/ampilova3.pdf (in Russian)

[4] Yong Xu, Hui Ji, Cornelia Fermuller, "Viewpoint Invariant Texture Description Using Fractal Analysis", Int. J. Comp. Vis, 2009, 83, p. 85-100.

[5] Ashvin B. Chhabra, Charles Meneveau, Roderick V. Jensen and K. R. Sreenivasan. "Direct determination of the f(α) singularities spectrum and its application to fully developed turbulence", Physical Review A, Volume 40, Number 9, November 1, 1989. p. 5284-5294.

[6] N. Ampilova, V. Sergeev, I. Soloviev. "On some questions concerning to the multi-fractal spectra calculation", Proc. 10 Int. Conf. CEMA15, 15-17 Oct. 2015, Sofia, Bulgaria. p. 14-17.

[7] N. Ampilova, I. Soloviev, J. Barth. "Application of fractal analysis methods to images obtained by crystallization modified by an additive", Journal of Measurements in Engineering, Vol. 7, Issue 2, 2019, p. 48-57. https://doi.org/10.21595jme.2019.20436.

COMPUTER MODELING OF THE MOTION OF CHARGED PARTICLES IN LOW FREQUENCY ELECTROMAGNETIC FIELD (selected from CEMA'19 Conference)

M. Syasko, I. Soloviev

St. Petersburg State University, Comp. Sci. Dept.

St. Petersburg, Russia

Email: st024504@student.spbu.ru, i.soloviev@spbu.ru

Abstract

The problem of computer modeling and visualization of low frequency electromagnetic fields is in the area of interest of such directions as education, research activity, medicine and industry. Visualization helps better understanding the influence of magnetic fields on various physical environments, and a clarifying the physical and mathematical models that are used. In industry visualization is often applied in the tools for non-destructive testing and in magnetic inspection systems. In medicine these fields are traditionally used in magnetotherapy, and at the moment computer modeling and visualization are often the only practical approach to the studying the influence magnetic fields on a living organism. In this work we demonstrate a computer tool both for modeling a magnetic field distribution and the motion of a charged particle in this field. The algorithms are implemented in a special environment Unity. That allows the combination of calculations and visualization and results in considerably lower run-time and the development of a flexible application that may be easily used by physicians. The results of the experiments are given.

1. INTRODUCTION

Computer modeling and visualization of low frequency electromagnetic fields are of interest to education, research activities, medical practice and industry. Visualization furnishes insights into the nature of the influence of magnetic fields on various physical environments, reveals peculiarities of emerging phenomena and in many cases helps to clarify the physical and mathematical models that are used. In industry such a visualization is often applied when elaborating tools for non-destructive testing [6]. Low frequency magnetic fields are also used in magnetic inspection systems.

Of special interest is the application of the methods of computer modeling and visualization in biology and medicine [1,5]. Experimental data show that low frequency electromagnetic fields may have a beneficial effect on the processes occurring in living systems. Over the past 20 years magnetobiology [4] is progressing rapidly. This branch of biology originates from biophysics and contributes to the elaboration of the methods of treatment of various deceases. In particular, in medicine the magnetotherapy method is widely used, and in this case the modeling and visualization of magnetic fields help to set and control the device parameters. That results in increasing effectiveness and safety of curative sessions.

Computer modeling and visualization of low frequency magnetic field in a magnetotherapy device was performed in [2, 7], where the calculations were made for a given configuration of coils in 3D space. The calculation of magnetic induction was performed in the points of a given space grid and to obtain the induction value in an arbitrary point, various methods of interpolation were used. In view of the large volume of calculation several types of optimization were implemented. Basing on the obtained results the authors of [3,9] developed an application for modeling the motion of a charged particle in the low frequency magnetic field generated by a given configuration of coils. In all the papers visualization was performed with using Paraview software, which complicated the technology considerably.

Thus, at the moment there is a program software for calculation and visualization of the magnetic field generated by different configurations of coils used in magnetotherapy devices, and the modeling of the motion of a charged particle in this field. The main problem is the authors used specialized graphic packages to visualize the results of calculation. Such an approach complicates the practical using of the software implemented, because a user has to organize file transfer between different program systems "by hand".

In this work we present a more flexible variant of the solving the problem above, which combines both all the calculations and visualization in one environment. Besides that, a new algorithm for calculation and visualization of low frequency magnetic field is designed and implemented. It is based on the fact that in any point of the field the magnetic induction vector lies on the tangent to a magnetic field line. So, we do not use a

predefined space configuration for the lattice of points, but being in a given point we obtain the next point for calculation by moving along the tangent on a small distance h. On this approach we do not need to use an interpolation, which leads to a reducing run-time.

In our study we have implemented an approach where the calculation of the field and trajectories of charged particles and the visualization of the results are performed in a uniform programming environment — the cross-platform software package Unity [10,11]. This environment is widely used for design of the projects with step-by-step improvement, for example in the cycles of prototyping or testing. There is a wide range of tools for the editing objects in the built-in editor and tuning the editor by using a scenario which adds new functional peculiarities and control elements.

Unity applications can be deployed to any desktop or mobile platform with little optimization and minor changes in code. This technique allowed us to optimize resource–intensive mathematical operations, which led to an optimization as a whole.

The system assumes further development. It is planned to visualize the motion of a charged particle in various physical environments, to improve the interface, the editor for the environment, coils and charged particles. The implemented program product may be easily used by physicians for study the results of magnetotherapy for various parameters of physiotherapy devices.

The paper is organized as follows. The next section contains a brief description of the mathematical model and algorithms for its solving. In section 3 the description of Unity environment is given. The last section shows the results of experiments.

2. MATHEMATICAL DESCRIPTION OF THE MODEL

2.1 Magnetic field calculation

Our model includes the calculation of the low-frequency magnetic field generated by one or several coils which are placed in the space according to a given configuration and the modeling of the motion of a charged particle in this field. The first problem is well known model task, and the calculation is performed in the cylindrical system of coordinates by the formulas using elliptic integrals. In the process of calculation, we have to use the Cartesian coordinates, so the transitions between two systems are performed.

The magnetic field is traditionally calculated in the points of a given space grid, so in an arbitrary point an interpolation is performed. This way of solving was due to the fact that for visualization a special software was used, which required the array of values of magnetic inductions in a lattice given. This approach was implemented in our previous works [2,3,7,9]. In this paper we propose a new method in which we construct the grid on a section plane. Each vector of magnetic induction in a point M lies on the tangent to the magnetic field line passing through M, hence we start from a point of the grid, calculate the magnetic induction and obtain the next point as the point on the tangent on a given distance from the initial point M. The implementation of such an algorithm became possible in the special environment which unites calculations and visualization.

In the modeling of the charged particle motion we use the second law of Newton, being the Lorentz force acting on the particle. We use the second order system of difference equations which is obtained by application of the method of central differences for derivatives. Such an approach leads to more effective results and does not require using software packages. As these tasks were discussed in papers [2,3] in details, we give here only main formulas for easier understanding.

The scheme for calculation of magnetic field for one contour of a coil is shown on Fig. 1.

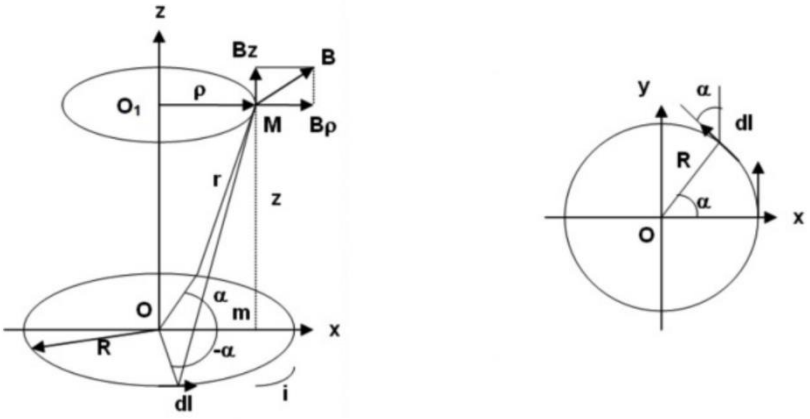

Fig. 1. Calculation of magnetic induction in a point M on a contour.

Here magnetic field lines are in the plane passing through the axis Oz. The magnetic induction vector $\vec{B}_M$ in a point M is defined by scalar components $B_\rho = rot_\rho A$ and $B_z = rot_z A$, (as $B_\alpha = 0$) and are calculated as

$$B_\rho = \frac{\mu_0 i}{2\pi} \frac{z}{\rho\sqrt{(R+\rho)^2+z^2}} \left(\frac{R^2+\rho^2+z^2}{(R-\rho)^2+z^2} L - K\right), \quad (1)$$

$$B_z = \frac{\mu_0 i}{2\pi} \frac{1}{\sqrt{(R+\rho)^2+z^2}} \left(\frac{R^2-\rho^2-z^2}{(R-\rho)^2+z^2} L + K\right). \quad (2)$$

where *L* and *K* are elliptic integrals of the first and second type.

For an arbitrary configuration of coils the value of magnetic induction in a point M is calculated as the sum of magnetic induction taken over all the contours (using formulas 1,2) of all the coils, and all needed coordinate transformations are performed. All these actions are collected in a program block (procedure) *MagnIndPoint()*.

2.2 Visualization of magnetic field

The algorithm for calculation of magnetic induction is the follows.

a) Chose a plane containing OZ axis and orthogonal the plane XY.

b) Construct a lattice of points (M_i) in the given part of this plane and calculate the magnetic inductions vectors B_{M_i}.

c) Let $M(x, y, z)$ be a point of the lattice and B_M be the magnetic induction vector in M. This point lies on a magnetic field line and B_M is on the tangent in this point to the line. The directing vector of the tangent is defined by the coordinates(B_x, B_y, B_z). To obtain the next point for calculation of magnetic induction we take the point $M_1(x_1, y_1, z_1)$ on the tangent which is on a small distance h from $M(x, y, z)$. The coordinates of $M_1(x_1, y_1, z_1)$ are found from the system

$$\frac{x_1-x}{B_x} = \frac{y_1-y}{B_y} = \frac{z_1-z}{B_z},$$

$$(x_1-x)^2 + (y_1-y)^2 + (z_1-z)^2 = h^2.$$

Thus, we have

$$x_1 = x \pm \frac{hB_x}{\alpha(x,y,z)}, \; y_1 = y \pm \frac{hB_y}{\alpha(x,y,z)}, \; z_1 = z \pm \frac{hB_z}{\alpha(x,y,z)},$$

where

$$\alpha(x, y, z) = \sqrt{B_x^2 + B_y^2 + B_z^2}.$$

We take both values for (x_1, y_1, z_1) and repeat the calculations from item a). The construction is completed when we come to the boundary of the given area or the number of steps is achieved. The number of section planes is a parameter of the program.

2.3 Motion of a charged particle

In what follows we used the mathematical model that includes the action of electric field as well. The detailed derivation of equations for the movement of charged particle in electric and magnetic fields is given in many textbooks, for example in [8]. We describe them briefly. Let q and m be charge and mass of a particle. Denote by $\vec{E}(x, y, z, t)$ and $\vec{B}(x, y, z, t)$ the intensities of electric and magnetic field induction in the point (x, y, z) at the moment t. The force acting the ion in electrical field is equal to $q\vec{E}$, and the Lorentz force in magnetic field equals $q\vec{v} \times \vec{B}$. Writing the second law of Newton we obtain $m\frac{d\vec{v}}{dt} = q(\vec{E} + \vec{v} \times \vec{B})$. Assuming that $\vec{B}$ is co-directed with Oz, and hence $B_z = B, B_x = B_y = 0$, we obtain the following system of equations:

$$\begin{aligned} m\ddot{x} &= q(E(x, y, z, t)sin\gamma cos\beta + \dot{y}B(x, y, z, t)) \\ m\ddot{y} &= q(E(x, y, z, t)sin\gamma sin\beta - \dot{x}B(x, y, z, t)) \\ m\ddot{z} &= qE(x, y, z, t)cos\gamma \end{aligned} \tag{3}$$

The above system was investigated in [3, 9] and the algorithm for approximate calculation based of using difference equations was proposed and implemented. The second order discrete system obtained from (3) has the form:

$$\begin{aligned} x_{i+1} - K_i y_{i+1} &= 2x_i - x_{i-1} - K_i y_{i-1} + L_i sin\gamma cos\beta \\ K_i x_{i+1} + y_{i+1} &= 2y_i - y_{i-1} + K_i x_{i-1} + L_i sin\gamma sin\beta \\ z_{i+1} &= 2z_i - z_{i-1} + L_i cos\gamma \end{aligned} \tag{4}$$

where $K_i = \frac{qh}{2m}B(x_i, y_i, z_i)$ if current is constant, and $K_i = \frac{qh}{2m}B\cos\omega t_i$ in the case of variable current with frequency ω. By analogy $L_i = \frac{qh^2}{m}E(x_i, y_i, z_i)$, if electrical field depends on the point, and $L_i = \frac{qh^2}{m}E\cos\omega t_i$ for periodic field. The system (4) is linear, z_i are calculated independently from x and y, and on every step x_{i+1}, y_{i+1} may be found by the Cramer method, because the determinant of the system $\Delta = 1 + K_i^2 \neq 0$.

Then, in our work we realized this algorithm in Unity engine. The initial data are parameters of a particle q and m, the initial points $M_0 = (x_0, y_0, z_0)$, $M_1 = (x_1, y_1, z_1)$ (in global Cartesian coordinate system) of the trajectory and values of magnetic induction in these points. For each point of the trajectory the magnetic induction is calculated by the program *MagnIndPoint()*.

3. TECHNOLOGICAL TOOLS OF THE MODELING

3.1 Short description

Unity environment is a cross-platform tool for development of 3D applications. Such applications may be set practically on all known platforms [11]. Unity supports DirectX and OpenGL, which results in obtaining high-level solutions by the use of modern graphical tools.

Unity also supports script languages, so the programming in this system should present no problems because there is no need to use a large number of extraneous solutions. In the kernel of Unity there are many built-in additional tools for design, so the programming in the environment is simple and clear enough.

The working process is affected by way of the Unity visual editor. The editor links scenes, and combines the project resources and the code into interactive objects, which allows optimizing the process of implementation of professional visual applications. It should be noted that in this environment a flexible approach to object-oriented programming is realized: objects are created by union but inheritance, and there are the links controlled between the objects.

3.2 Optimization

To optimize the calculation of magnetic induction we at first splat into streams the calculation of coordinates and magnetic induction. Then we splat the calculation of functions, magnetic induction for all the contours of a coil, total value of magnetic induction in a point, coordinate transformations and visualization. Depending on a system configuration such an optimization leads to the reducing run-time approximately 7 – 8 times. For a system of 3 coils (10 contours) the run time before optimization is 3 – 4 min, after optimization 25 – 30 sec.

4. NUMERICAL EXPERIMENTS

Device parameters are the following: current intensity is $3A$, coils have 7 turns, the number of windings is 25. The size of the region (in mm) is 600x600x300, the step on time h (in sec) is 10^{-6}.

The numerical experiments were performed for various types of ions and combination of magnetic and electrical fields. For different configuration of magnetic field (without electric one) the motion of 3 particles:

$$Na^{+}: q = 3.817 * 10^{-26}, m = 1.60217 * 10^{-19};$$

$$SO_4^{-}: q = -7.634 * 10^{-26}, m = 1.59468 * 10^{-22}$$

$$e: q = -1.602 * 10^{-19}, m = 9.1 * 10^{-31}$$

were modeled. All the particles start the motion from the initial point (5,10,15). On Figs. 2 – 3 the motion of the particles is shown for different position of coils. Fig. 4 shows the motion of Na ion from the point (0,0,0) when electric field is added.

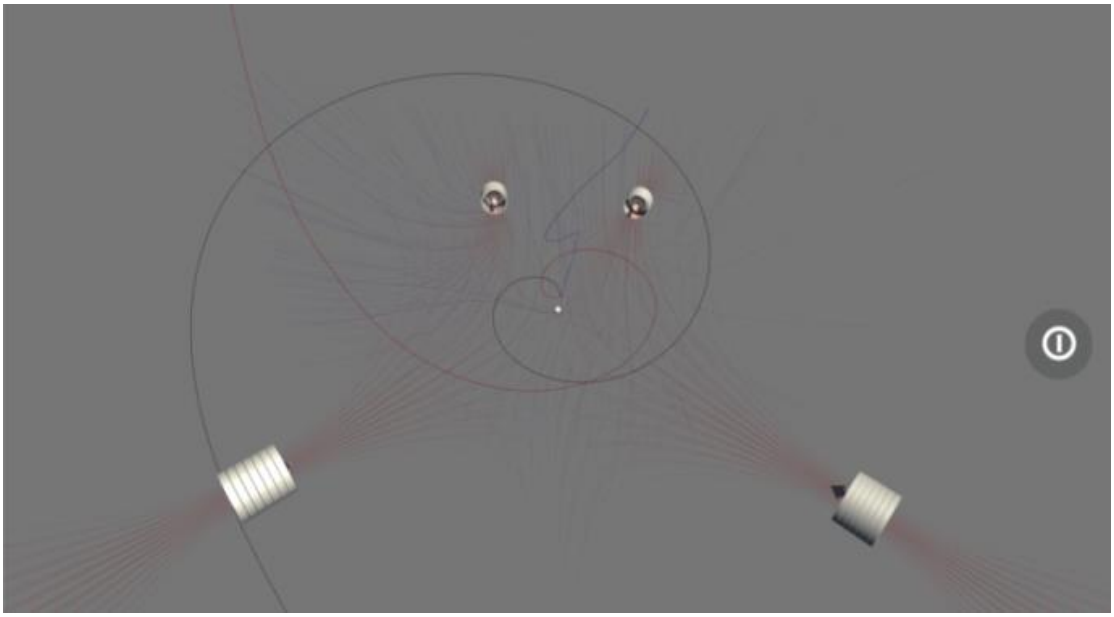

Fig. 2. Four coils with coordinates (-272, 0, -272), (141, 0, 332), (-130, 0, 348), (284, 0, -284).

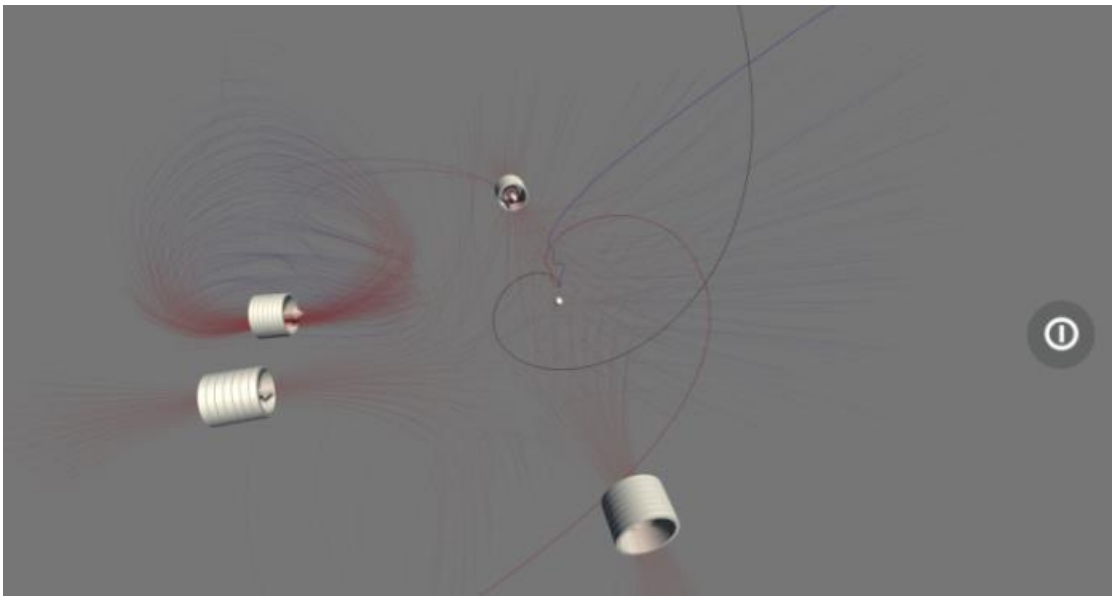

Fig. 3. Four coils with coordinates (-331, 0, -74), (0, 0, 317), (-322, 0, 51), (284, 0, -280).

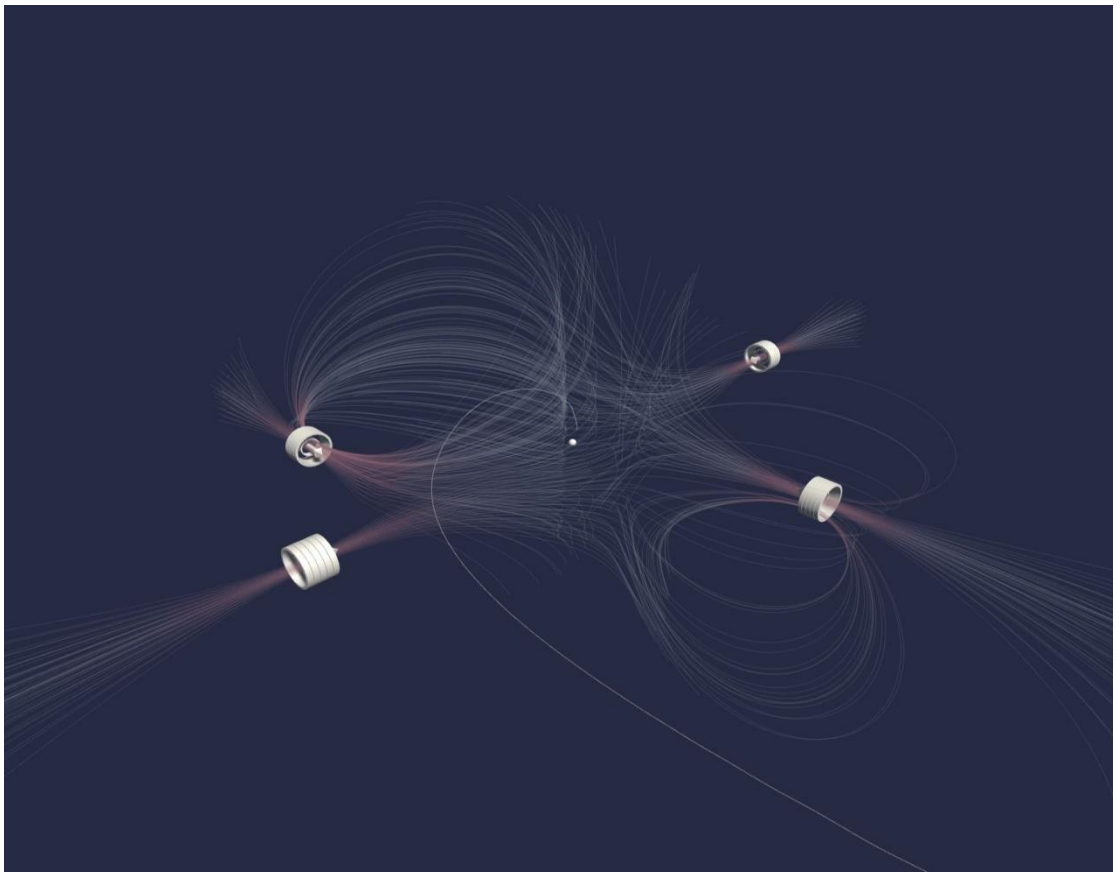

Fig. 4. Four coils with coordinates (-257, 0, -257), (293, 0, 293), (-325, 0, -10), (273, 0, -137). Electric intensity is 30v/m, $\beta = 60^{\circ}, \gamma = 55^{\circ}$.

5. CONCLUSION

Development of tools for computer modeling of magnetic field distribution and the motion of various particles in the field is the important task which may help in studying the influence of low frequency magnetic field on living tissues and estimate the effectiveness of various curative sessions. Further investigations lead to a natural using other mathematical models which may be applicable not only for air but for different environments as well.

REFERENCES

[1] V. Aleksandrov. "Electromagnetic fields and ecology", St. Petersburg, 2005. (in Russian).

[2] N. Ampilova, D. Dimitrov, B. Kudrin. "Mathematical modeling of low frequency magnetic field in systems for magnetotherapy", Proc. 8 Int. Conf. CEMA13, Sofia, Bulgaria, October 17-19, 2013, p. 48-51. ISSN: 1314-2100, Pub. KING 2001, Sofia

[3] N. Ampilova, F. Uvarichev, I. Soloviev. "On the estimation of magnetotherapy curative sessions effects", Proc. 13 Int. Conf. CEMA18, 18-20 Oct. 2018, Sofia, Bulgaria, p. 62-65, ISSN: 1314-2100, Pub. KING 2001, Sofia.

[4] V. Binhi. "Magnetobiology: Underlying physical problems", San Diego, Academic Press, 2002.

[5] V. Binhi, A. Savin. "Effects of weak magnetic fields on biological systems: physical aspects", PHYS-USP, 2003, 46 (3), p. 259–291.

[6] N. Ida. "Numerical modelling for electromagnetic non-destructive evaluation", New-York, Springer Publishing Company, 1994.

[7] B. Kudrin, I. Soloviev. "On interpolation methods of low frequency magnetic field in systems for magnetotherapy", Proc. 9 Int. Conf. CEMA14, Sofia, Bulgaria, October 16-18, 2014, p. 154-157.

[8] B. Lennert, "Dynamics of charged particles", North Holland, 2004.

[9] F. Uvarichev, N. Ampilova, I. Soloviev. "On the modeling ion motion in electromagnetic field", Proc. 10 Int. Conf. EPE-2018, ID 2627, p.1-4, ISBN 978-1-5386-5061-5 IEEE Catalog number CFP 1847S-USB.

[10] Unity. URL: https://unity.com

[11] Unity Multiplatform. URL: https://unity3d.com/unity/features/multiplatform.